bioRxiv preprint doi: https://doi.org/10.1101/255695; this version posted January 29, 2018. The copyright holder for this preprint (which was not certified by peer review) is the author/funder. All rights reserved. No reuse allowed without permission.

# Sub-voxel light-sheet microscopy for high-resolution, high-throughput volumetric imaging of large biomedical specimens

Peng Fei[1,2+*], Jun Nie[1+], Juhyun Lee[3,5+], Yichen Ding[3,4+], Shuoran Li[6], Zhilong Yu[9], Hao Zhang[1], Masaya Hagiwara[7,8], Tingting Yu[2], Tatiana Segura[6], Chih-Ming Ho[8], Dan Zhu[2] and Tzung K. Hsiai[3,4*]

[1] School of Optical and Electronic Information, Huazhong University of Science and Technology, Wuhan, 430074, China.

[2] Britton Chance Center for Biomedical Photonics, Wuhan National Laboratory for Optoelectronics, Huazhong University of Science and Technology, Wuhan, 430074, China.

[3] Department of Bioengineering, University of California, Los Angeles, Los Angeles, 90095, U.S.A.

[4] School of Medicine, University of California, Los Angeles, Los Angeles, 90095, U.S.A.

[5] Joint Department of Bioengineering of UT Arlington/ UT Southwestern, University of Texas at Arlington, Arlington 76010, U.S.A.

[6] Chemical and Biomolecular Engineering Department, University of California, Los Angeles, Los Angeles, 90095, U.S.A.

[7] Nanoscience and Nanotechnology Research Center, Research Organization for the 21st Century, Osaka Prefecture University, Osaka, 599-8570, Japan.

[8] Mechanical and Aerospace Engineering Department, University of California, Los Angeles, Los Angeles, 90095, U.S.A.

[9] College of Engineering, Peking University, Beijing, 100871, China.

[+] These authors contribute equally to this work

A key challenge when imaging whole biomedical specimens is how to quickly obtain massive cellular information over a large field of view (FOV). Here we report a sub-voxel light-sheet microscopy (SLSM) method that enables high-throughput volumetric imaging of mesoscale specimens at cellular resolution. Unlike either stepwise z-scan or

bioRxiv preprint doi: https://doi.org/10.1101/255695; this version posted January 29, 2018. The copyright holder for this preprint (which was not certified by peer review) is the author/funder. All rights reserved. No reuse allowed without permission.

stitching of multiple small blocks, this method applies a non-axial, continuous scanning strategy, rapidly acquiring a stack of large FOV images with 3-D nanoscale shifts encoded. By adopting a sub-voxel-resolving procedure, SLSM method models these low-resolution, cross-correlated images in spatial domain and iteratively recovers a 3-D image that encompasses improved resolution throughout the entire sample. It can surpass the optical limit of a conventional macro-view light-sheet microscope over 3 folds while achieve a high speed of gigavoxels per minute. As demonstrated by the quick reconstruction of various samples, such as 3-D cultured cells, intact mouse heart, brain and live zebrafish embryo, SLSM method circumvents the tradeoff between *intoto* mapping of large-scale tissues (>100 $mm^3$) and isotropic imaging of single cells (~1 μm resolution). It eliminates the need of complicated mechanical stitching or precisely-modulated illumination, using a simple light-sheet setup and fast GPU-based computation to address the general challenge of high-throughput, high-resolution 3-D microscopy that is originally coupled to the physical limitation of system's optics.

In optical microscopy, high-resolution volumetric imaging of thick biological specimens is highly desirable for many biomedical applications such as development biology, tissue pathology, digital histology and neuroscience. To interrogate cellular events from the entire organisms, e.g., live embryo, intact tissue and organ, spatiotemporal patterns spanning from micro- to meso-scale need to be *intoto* followed and analyzed[1-5]. As a result, there is a growing need to develop high-resolution, high-throughput imaging methods that can map entire large-volume specimens at high spatiotemporal resolution[6,7]. Light-sheet microscopy (LSM) has recently emerged as a technique of choice that can image samples with low phototoxicity and at high speed[8-23]. Similar to conventional epifluorescence methods, LSM is still subject to the fundamental tradeoff between the high illumination/detection numerical apertures (NA) and wide imaging FOV. In addition, accurate digital sampling by the camera is also compromised by the need of large pixel size with a high fluorescence sensitivity. Therefore, the achievable resolution of current LSM system is often pixel-limited under large FOV, resulting an inadequate optical throughput for digitally imaging mesoscale

bioRxiv preprint doi: https://doi.org/10.1101/255695; this version posted January 29, 2018. The copyright holder for this preprint (which was not certified by peer review) is the author/funder. All rights reserved. No reuse allowed without permission.

organisms at cellular resolution. Development of tile imaging-based LSM systems has been prompted to artificially increase the space-bandwidth product (SBP) of an imaging system[24], realizing high resolution imaging of large specimens[18,25-29]. Despite the compromised speed by repetitive mechanical stitching, the high NA illumination/detection configuration in tile imaging induces increasing phototoxicity for increasing size of sample, and limits the fluorescence extraction from the deep of tissues. Several approaches, such as fourier ptychographic microscopy[30,31], synthetic aperture microscopy[32-35], contact-imaging microscopy[36,37], wavelength scanning microscopy[38], and lens-free digital holography[39-41] have recently provided a computational way to reconstruct a wide field-of-view, high-resolution image based on a number of low-resolution frames that contains certain correlations in space, frequency or spectrum domain[42-44]. However, most of these methods aim for two-dimensional bright-field microscopy, not compatible with volumetric fluorescence imaging of thick samples. Here we present a new imaging method that is capable of providing three-dimensional super-resolution and increased SBP for conventional light-sheet microscopy, without the involvement of mechanical stitching or complicated illumination modulation. This method, termed sub-voxel light-sheet microscopy (SLSM), shares its roots with those pixel super-resolution (PSR) techniques[36,37,41-43,45], working by efficiently computing a number of low-resolution, under-sampled and shift-modulated LSM volumes in spatial domain, to reconstruct an output with significantly higher resolution throughout the entire sample. But unlike either PSR or conventional LSM, our SLSM method for the first time super-resolve the large-scale, fluorescence images in term of voxel, expanding the system's SBP originally limited by the low magnification/NA optics. Furthermore, in SLSM, these special image sequences carrying high-frequency spatial information can be obtained by a simple retrofit of z-scan apparatus in conventional LSM systems. At the same time, the segmentation of the raw image sequence, the modeling of the spatial shifts beyond the system resolution, and finally the reliable estimation of the high-resolution output, are all based on a GPU-accelerated, parallel computation flow. The rapid-and-convenient generation of raw image data, in conjunction with efficient image modeling and reconstruction, together

bioRxiv preprint doi: https://doi.org/10.1101/255695; this version posted January 29, 2018. The copyright holder for this preprint (which was not certified by peer review) is the author/funder. All rights reserved. No reuse allowed without permission.

realize the high-throughput, high-resolution imaging of large biological specimens. This capability of SLSM has been widely verified through the imaging of various samples, such as 3-D cultured cells, live zebrafish embryo and intact mouse organs. In addition, we demonstrate SLSM can be combined with multi-view data fusion[46] to achieve complete imaging of scattering samples, with realizing an isotropic resolution ~1.6 μm (compared to originally ~ 6.5 μm and 26 μm) throughout an over 100 $mm^3$ volume. In the following, we will elucidate the SLSM experimental set-up, discuss how to implement the sub-voxel-resolving reconstruction and demonstrate the applications in whole organisms imaging.

**Off-detection-axis scanning set-up.** SLSM imaging is implemented based on a home-built selective plane illumination microscope (SPIM), which is a well-known modality of LSM (see Methods and Supplementary Fig. S1 for full optical layout). It works under a low-magnification setup with a wide FOV covering the entire specimens. Unlike regular SPIM with z-scan parts, SLSM additionally contains a customized tilting plate that can adjust the scanning axis, allowing samples to be scanned along a direction with certain deviation angle $\theta$ to the z axis (detection axis) (Fig. 1a). As sample being continuously moved across the laser-sheet along this non-detection-axis direction, a camera records the images of the sequentially-illuminated planes at high acquisition speed (Fig. 1b). Then by matching the frame rate $r$ and scanning velocity $v$, a fine step size $s$, typically hundreds of nanometers ($s = v/r$), is generated between adjacent frames (Fig. 1b). Every non-axial incremental step as such provides unit sub-voxel shift components $s_x$, $s_y$ and $s_z$ simultaneously in both lateral and axial directions, through a one-directional scan (Fig. 1b). In addition, this continuous scanning mode matched by fast camera acquisition provides SLSM a high imaging throughput up to hundreds of megavoxels per second. Varying from the sample size as well as the fluorescing intensity, the SLSM acquisition usually takes only a few seconds to a few minutes, with finally generating a raw image stack containing thousands of spatially-modulated frames.

bioRxiv preprint doi: https://doi.org/10.1101/255695; this version posted January 29, 2018. The copyright holder for this preprint (which was not certified by peer review) is the author/funder. All rights reserved. No reuse allowed without permission.

**Principle of sub-voxel-resolving procedure**. A sub-voxel-resolving (SVR) algorithm is designed to specifically segment the acquired shift-encoded, wide-view, low-resolution image stack (denoted as $\underline{P}$) into multiple sub-stacks, model them as probability distributions with subtle spatial correlations, and reconstruct a final output image that encompasses significantly improved resolution over the entire large-volume sample (Fig. 1c). The raw image stack $\underline{P}$ is first divided into a number of low-resolution (LR) 3-D images $\underline{P}_k$ ($k$ = 01, 2,…,$n$). In each low-resolution $P_k$, the voxel width $w$ (x, y) is simply given by the division of camera pitch size and magnification factor. The voxel depth $d$ that denotes axial spacing we make when extracting the slices from the raw stack, is set to be around a third of the laser-sheet's longitudinal extent $l$ ($1/e^2$) to meet the Nyquist sampling principle. The segmentation is therefore done by re-slicing the raw image every $l/3s_z$ frames, as shown in Fig. 1b and Fig. 1c, step 1. The number of total LR images $n$, which implies how much sub-voxel information we can extract from the raw image, is determined through dividing one LR voxel width $w$ by the unit lateral shift $s_x$, indicating this amount of images are correlated with each other in term of sub-voxel-resolution displacements (Fig. 1b, c). Each segmented low-resolution $\underline{P}_k$ can be considered as a blurred and under-sampled "regular SPIM" image with presenting standard resolutions accepted from the system optics. Meanwhile, all the $P_k$ can be spatially registered to a high-resolution (HR) image $\underline{I}$ we are about to solve (also the reference image $P_1$) with a non-axial, sub-voxel-resolution shift $s_k = (k-1) * s$ (Fig.1c, red, green, purple-bordered images). SVR procedure then reconstructs the HR $\underline{I}$ based on the computation of these LR images modeled with their known sub-voxel shifts, system's optical blurring and camera's discretization.

The design of SVR follows a straightforward principle as the pixel super-resolution techniques function in 2-D spatial domain[36,42]: seeking for a super-resolved estimate $\underline{I}$ that is most consistent with multiple measurements $\underline{P}_k$ after a series of degradation operators that reasonably models the digital imaging process being successively applied[36,43]. Here $\underline{I}$ can be specifically solved via minimizing the following cost function:

bioRxiv preprint doi: https://doi.org/10.1101/255695; this version posted January 29, 2018. The copyright holder for this preprint (which was not certified by peer review) is the author/funder. All rights reserved. No reuse allowed without permission.

$$\hat{\underline{I}} = \underset{\underline{I}}{ArgMin}\left[\sum_{k=1}^{n}\rho(P_k, D_k O_k S_k \underline{I})\right] \qquad (1)$$

in which $\rho$ is measuring the difference between the model and measurements. $S_k$ is the geometric motion operator between HR estimate $\underline{I}$ and $k^{th}$ LR $\underline{P}_k$, the point-spread-function of SLSM system is modeled by the blur operator $O$, and $D_k$ represents the decimation operator that models the digital sampling of camera. Theoretically, the computation estimates a HR image which has maximum likelihood with the LR inputs after given degradations $S_k$, $O_k$, and $D_k$ applied. Fig. 2c, step 2 shows an iterative maximum likelihood estimation (MLE) solving procedure of $\underline{I}$. The program first generates an initial guess of HR $\underline{I}$ ($\underline{I}_1$), which is simply the interpolation of $\underline{P}_1$. Each LR image $P_k$ is then compared to the warped, blurred and decimated $\underline{I}_1$ using gradient back-projection operator (block $G_k$). Their differences are summed and thereafter weighted by a factor $\beta$, for the calculation of the 2nd estimate. This process is iterated until a converged solution of $m^{th}$ $\underline{I}$ is approached after feeding the $(m\text{-}1)^{th}$ estimate. A voxel re-alignment is applied at the final step to recover an accurate reconstruction from slight deformation caused by the non-axial scan (step 3). The detailed implementation of SVR procedure is elucidated in Supplementary Notes and Supplementary Fig. S4, with the simulation results shown in Supplementary Fig. S7. The optimization of the SVR parameters are discussed in Supplementary Fig. S5 and 6.

## Results

**Imaging characterization.** Simulation results of the proposed SVR procedure are provided in Supplementary Fig. S7, whereas Fig. 1d to 1f experimentally characterize the performance of SLSM through imaging fluorescent microbeads (~500 nm diameter), under a 4×/0.13 detection objective (DO) plus 0.022 NA plane illumination (PI) configuration. The microbeads are scanned along a $\theta$ angle of 10 degrees (to y-z and x-z plane) with step-size $s$ of 144 nm, resulting an incremental lateral shift $s_x$ and axial shift $s_y$ of 25 nm and 140 nm, respectively. Then 65 groups ($n$) of low-resolution (LR),

bioRxiv preprint doi: https://doi.org/10.1101/255695; this version posted January 29, 2018. The copyright holder for this preprint (which was not certified by peer review) is the author/funder. All rights reserved. No reuse allowed without permission.

3-D images (voxel size 1.625 by 1.625 by 6 μm) are extracted from the raw sequence to compute a sub-voxel-resolved image with 4 times enhancement at each dimension. The LR and SVR results are compared to mid-magnification SPIM (10×/0.3 DO/0.04 NA PI), high-magnification SPIM (20 × /0.45 DO/0.06 NA PI) and confocal microscope (20×/0.7 objective), as shown in Fig. 1d. The line intensity profiles of the resolved beads are plotted in Fig.1e and 1f, to compare the lateral and axial resolutions of these methods. The achievable lateral and axial FWHMs of 4×-SLSM are improved from ~4 and 13 μm to ~1.2 and 4.5 μm, respectively, which are similar to those of 20 ×-SPIM and 20×-confocal.

We validate the SLSM by obtaining high-resolution reconstruction of 3D-cultured normal human bronchial epithelial (NHBE) cell spheroids (labelled with DAPI nucleic acid staining, Methods section), as shown in Fig. 2a. A sequence of images from consecutively-illuminated planes are rapidly recorded in 1 minute under an acquisition rate of 100 fps, targeting a specific volume-of-interest contains dense cell spheroids (Fig. 2a). Each LR image subdivided from the raw stack simply accepts the limited resolution from the system optics, hence only the rough shape and distribution of the selected spheroid are identified whereas the single cells remain unresolvable (Fig. 2b1). SVR procedure then starts with an initial guess which is simply a ×4 interpolation of the 1st reference image (Fig. 2b2), and iteratively converges to the final HR image with the chromatins inside cell nucleus becoming distinguishable (Fig. 2b3). Indeed, the linecuts through the cell spheroids (Fig. 2d) by each method reveal substantially improved resolution from SVR, which surpasses 20×-SPIM result that suffers from observable spherical aberration (Fig. 2c, Supplementary Fig. S3). Besides the selective image planes, we compare the volume rendering of a reconstructed cell spheroid between conventional 4×-SPIM and 4×-SLSM, explicitly showing a much improved 3-D localization of single cells (Fig. 2e). SLSM provides a wide FOV of ~23 $mm^2$ from its low magnification DO (4×/0.13) and low NA PI (0.022), whereas its achieved resolutions are similar to those of 20×-SPIM (20×/0.45 DO / 0.07 NA PI). It thus can be considered as a light-sheet microscope that combines the FOV advantage of 4×-

bioRxiv preprint doi: https://doi.org/10.1101/255695; this version posted January 29, 2018. The copyright holder for this preprint (which was not certified by peer review) is the author/funder. All rights reserved. No reuse allowed without permission.

SPIM with resolution advantage of 20×-SPIM. From another perspective, its stitching-free, continuous scanning mode exhibits a much higher acquisition throughput as well as lower photo-bleaching than those stitching results of 10×-SPIM, 20×-SPIM and confocal microscope (Supplementary Notes). We calculate the imaging resolution, speed and photobleaching of 4×-SPIM, 10×-SPIM tile imaging, 20×-SPIM tile imaging, 20×confocal and 4×SLSM. As indicated in Fig. 2f, SLSM yields a highest effective throughput at ~25 mega voxels SBP per second, which is over 10 times higher than other modalities. Besides the increased space-band-width product (FOV divided by resolution), the SVR computation, to some weak fluorescing extent, improves the signal-to-noise ratio after multiple image fusion (Supplementary Fig. S8). Furthermore, circumventing the use of high NA, high-maintenance optics renders SLSM much less vulnerable to chromatic aberration existed in multi-color illumination (Supplementary Notes and Supplementary Fig. S2) and resistant to the spherical aberration that causes severe image deterioration in the deep tissue (Supplementary Fig. S3). In the following applications, these underlying robustness allows SLSM prototype to image thick specimens at high spatial-temporal performance while keep a relatively simple set-up.

**Multi-color three-dimensional imaging of whole organisms at high-throughput.** SLSM doesn't require special engineering of fluorescence emission to generate image modulation, rendering it compatible with various labelling techniques. In Fig. 3, we demonstrate SLSM imaging of 2 types of specimens: an optically-cleared intact mouse heart (neonate, D2) that shows endogenous autofluorescence in cardiomyocytes (Fig. 3a), and a two-color tansgenetic zebrafish embryo (3 d.p.f.) tagged with green fluorescence protein at motor neurons (Islet1-GFP) and red fluorescence protein at somite fast muscles (mlcr-DsRed) (Fig. 3b). Furthermore, a time-course study on the anaesthetized live fish embryo from 48 to 72 h.p.f is implemented to investigate the neurons/muscles development in the hinderbrain region, as shown in Supplementary Fig. S10. The raw data acquisition is very fast at a rate over 200 megavoxels per second. Meanwhile, to match the high-speed acquisition, we develop a GPU-based parallel computation flow to greatly accelerate the SVR procedure at the same time, super-

bioRxiv preprint doi: https://doi.org/10.1101/255695; this version posted January 29, 2018. The copyright holder for this preprint (which was not certified by peer review) is the author/funder. All rights reserved. No reuse allowed without permission.

resolving the large-scale data at a high processing throughput over 100 megavoxels per second. As a result, SLSM is capable of rapidly imaging (acquisition + computation) these millimeter-size organisms at dozens of gigavoxel scale, providing super-resolved cellular structure-function information, such as myocardium architectures and interaction of developing motor neurons with somite muscles, in a few minutes to an hour. In Supplementary Fig. S11 and S12, SLSM has more broadly demonstrated its applications in whole organism imaging of Tg (clmc2:GFP) adult zebrafish heart (60 dpf) and $\alpha MHC^{Cre}$ ; $R26^{VT2/GK}$ murine heart (three colors, P1), which are otherwise spatially or temporally more challenging to regular light microscopes.

**Multi-view SLSM for isotropic super-resolution imaging of thick, scattering sample.** Despite the use of chemical clearing, light scattering from the deep of tissue still challenges the optical microscopy. Both laser excitation and fluorescence emission experience deflection and attenuation, which together deteriorate the signals severely. Meanwhile, even light-sheet imaging remains anisotropic, showing suboptimal axial resolution for several applications such as cell phenotyping and neuronal tracing. The advent of multi-view fusion method[46,47] addresses these issues. It works by registering, weighting and fusing a number of image stacks recorded under different views, and finally recovers a stack that shows complete signals with improved axial resolution. Here we demonstrate SVR procedure can be also combined with multi-view to *intoto* image thick and scattering samples at near isotropically improved resolution. We develop a 4-view SLSM prototype by imaging a Human Umbilical Vein Endothelial Cells (HUVEC) and Human Dermal Fibroblasts (HDF) 3-D sprouting network (Methods). The cells are co-cultured in a fibrinogen-based hydrogel mixed with dextran-coated Cytodex 3 microbeads (SiO2), finally forming a complex and light-scattering cellular network that contains Fibrinogen, HUVEC beads, and HDF cells. First, the sample is rotated 90° for each set of 2×-SLSM data acquisition (2×/0.06 detection, 0.015 NA sheet-illumination, 580 nm step-size, 7000 frames in 140 s), with totally 4 views of raw stacks obtained. Then each of them is sub-voxel-resolved separately based on 32 groups of segmented LR inputs, generating 4 views of

bioRxiv preprint doi: https://doi.org/10.1101/255695; this version posted January 29, 2018. The copyright holder for this preprint (which was not certified by peer review) is the author/funder. All rights reserved. No reuse allowed without permission.

anisotropic SVR image (4×4×2 enhancement). A multi-view registration followed by weighted fusion is included at the final step to produce an output image with isotropic sub-voxel resolution. This multi-view SVR (mv-SVR) workflow is further illustrated in Fig. 4a. In Fig. 4b, we compare the reconstructed volume renderings of $0^{\circ}$ SPIM image (1.1 gigavoxels, voxel size $3.25 \times 3.25 \times 9$ μm) and 4-view SLSM (190 gigavoxels, reconstructed voxel size 0.81 μm). Due to the strong scattering of fibrinogen-microbeads substrate, single view SPIM only visualizes an incomplete structure at poor resolution (Fig. 4b, left). 4-views SLSM, in contrast, reconstructs the entire sample with showing details of HUVEC sprouts from 2 adjacent dextran beads (Fig. 4b, right). High-resolution local views containing dense HDF fibers are provided in Fig. 4c and d, being compared to the single-view SPIM results as well. Besides the isotropically improved resolution (resolvable distance <1.6 μm, Fig. 4d inset) that enables clear identification of single sprouting HDF cells, the multi-view SLSM (mv-SLSM) also restores the highly light-scattered area in reference view (Fig. 4d, left). Given the fact that multi-view sub-voxel computation relies on the image registration and weighted fusion in Fourier space, the processing speed of 4-view-fused SVR is approximately an order lower than a single view's computation, on average reconstructing 18 megavoxels per second. With finally creating isotropic high-resolution, panoramic visualization that encompasses 190 gigavoxels across an over 100 $mm^3$ large volume (total processing time ~3 hours), mv-SVR procedure is able to accurately analyze vast amount of cells, such as sprouting branches and tip filopodia, over a piece of mesoscale tissue, providing solid foundation to explore mature vessel formation and vessel anastomosis processes, both of which are crucial for studying tissue regeneration.

**Fast quantitative mapping of neuronal networks in mouse brain.** We reconstruct a P30 Thy1-GFP-M mouse brain using 8 view-SLSM (Fig. 5a). High-resolution volumetric renderings of hippocampus (i), thalamus (ii), and cortex (iii) regions are shown as Fig. 5b, c and d, respectively. Compared to conventional SPIM with suboptimal qualities, 8 view-SLSM image resolves the fine neuronal sub-structures,

bioRxiv preprint doi: https://doi.org/10.1101/255695; this version posted January 29, 2018. The copyright holder for this preprint (which was not certified by peer review) is the author/funder. All rights reserved. No reuse allowed without permission.

such as dendrites and axons at an isotropic resolution of around 1 μm (350 gigavoxels SBP). Benefitting from remarkably improved visualization, neuronal subsets, such as clustered astrocyte neurons in thalamus region, can be segmented with their nerve fibers clearly separated (Fig. 5e, Imaris software). Three long-projection neurons are also successfully identified and registered in the P30 reference mouse brain. The pathways of these projection neurons are subsequently annotated according to standard mice brain atlas[48], as shown in Fig. 5e, ii, iii and iv. The high-resolution, high-throughput features of SLSM enables fast and accurate tracing of both the long-distance projections and the pathways within the neuronal circuits in the brain of a fluorescent protein transgenic mouse.

## Discussion

SLSM is based on an unconventional off-axis scan together with a sub-voxel reconstruction, to computationally surpass the resolution limit of a regular light-sheet microscope. It can be applied to most existing light-sheet microscopes by retrofitting with a readily available tilting stage, expanding the optical throughput for fast, high-resolution mapping of large biomedical specimens. In principle, the SVR procedure estimates a high-resolution 3-D image that best suits a certain conditional probability in spatial domain. As long as the aperture function and sub-voxel motion are accurately characterized, the maximum-likelihood link between the actual sample profile and recorded data allows SVR to iteratively render high-resolution image with a limited NA, under-sampled configuration that is originally incapable of providing such a small point-spread function as shown in Fig. 1. Unlike most super-resolution fluorescence microscopy methods that image a single cell beyond the diffraction limit by processing multiple frames acquired under large numerical aperture as well as highly specialized optics, SLSM is free from either illumination modulation or particular fluorescence labelling, designed to rapidly enhance the inadequate accuracy of unraveling large organisms under an ordinary small NA/large-view configuration. Its stitching-free, high-speed image acquisition followed by parallelized GPU processing flow provides

bioRxiv preprint doi: https://doi.org/10.1101/255695; this version posted January 29, 2018. The copyright holder for this preprint (which was not certified by peer review) is the author/funder. All rights reserved. No reuse allowed without permission.

super-resolved 3-D visualization at quasi-realtime throughput. Through imaging a variety of biological specimens from 3-D cells, developing embryos, to intact organs, our SLSM robustly shows improved performance at a low hardware and time cost, using efficient computation to circumvents the trade-off between larger imaging volume and more resolvable details. The ability to readily accomplish cellular imaging of mesoscale organisms at hundreds of gigavoxels SBP renders SLSM a valuable tool for wide biomedical applications such as development, histology, pathology and neuroscience, in which both large-scale statistics and high-resolution details are highly desired for mechanism study. In addition to single view mode, SLSM is also expandable through the combination with multi-view fusion. By a rational balance between higher throughput and more views, mv-SLSM can image thick-and-scattering samples with isotropic super-resolution and at moderately high throughput. More broadly speaking, this method is currently optimized for light-sheet microscopy which has relatively high image contrast and fast acquisition rate, while the nonaxial scan as well as SVR computation may be equally suited to other 3-D microscopy methods, such as confocal microscope and 3-D deconvolution microscope. Furthermore, we believe this sub-voxel imaging strategy could be more transformative as it provides a general iterative resolution recovery method that can be potentially applied to improve other 3-D imaging modalities which are possibly limited by inadequate sampling and poor focusing capability.

## Methods

**Experimental set-up.** A 4-wavelengths, fiber-coupled semiconductor laser (CNI Laser, RGB 637/532/488/405, China) was used as excitation source. The laser was first transformed into a collimated Gaussian beam with diameter ~8 mm ($1/e^2$ value). Then an adjustable mechanical slit (0-8 mm aperture) was used to truncate the beam along horizontal direction and thereby tune the aperture of plane illumination. The illuminating cylindrical lens (f = 40 mm) finally formed a wide laser-sheet that optically sectioned the large specimens with adjustable numerical aperture from 0 to 0.1. A ×2 or ×4 (Nikon Plan Apo Fluor 2×/0.06，4×/0.13 objetives) infinity-corrected, wide-field detection path is built orthogonal to the plane-illumination path, to collect the fluorescent signals. A 4 degrees of freedom motorized stage (x, y, z translation and rotation around y-axis, Thorlabs) integrated with a pair of customized tilting plates (10 degrees inclined surface) was built to mount the samples, scanning them across the laser-sheet along an off-detection-axis direction (Supplementary Fig. S1). For a given imaging

bioRxiv preprint doi: https://doi.org/10.1101/255695; this version posted January 29, 2018. The copyright holder for this preprint (which was not certified by peer review) is the author/funder. All rights reserved. No reuse allowed without permission.

configuration, the choice of the deviation angle $\theta$ was balanced between generating a small lateral shift component for larger enhancement factor and scanning a short axial distance when finishing an entire voxel shift. Usually, the diagonal of the LR voxel is chosen as the nonaxial scanning axis, with $\theta$ being 10 to 15 degrees. A sCMOS camera (Hamamatsu Orca Flash 4.0 v2 or Andor Zyla 5.5, pitch size 6.5 μm) continuously recorded the planar images from the consecutively illuminated planes at a high speed up to 200 frames per second.

**SPIM，SLSM and multi-view SLSM acquisition.** In conventional SPIM imaging, according to different illumination NA, sample was scanned along z-axis with 2 to 9 μm stepsize. To avoid the motion-blur happened in several microns' incremental move, z-scan need to be implemented in a step-by-step way via synchronizing the laser, motor and camera in Labview program. This stepwise z-scan limited the acquisition speed at a rate up to 13 fps in our system (Thorlabs stepper ZST225B). 10 × and 20 × tile SPIM imaging were automatically implemented in a z-x-y raster scanning way, and the acquired mosaic volumes were subsequently stitched together using Grid/Collection stitching plugin (ImageJ software). Since each time only a small region of entire illuminated plane was imaged, tile imaging was subjected to a photobleaching rate higher than SPIM and SLSM. For SLSM imaging, the camera was synchronized with continuous sample scan via Labview control, recording images under sequential mode. The step-size thus could be determined by the match of scanning velocity (10-30 μm/second) and camera's frame rate (20-200 fps). Depending on the sample dimension, tilted angle, and the enhancement factor, this value varied from 140 nm to 600 nm. Compared to the voxel size of several microns in the segmented LR volumes, motion-blur caused by the continuous scan was negligible under a such small step-size and didn't affect the accuracy of SVR computation. At the same time, the image acquisition of SLSM could be fast under continuous mode, taking 30 to 300 seconds to obtain a sequence containing thousands to tens of thousands of frames. For multi-view imaging, the stepper rotates the thick and scattering samples 4 to 8 times, with acquiring a number of raw SLSM image stacks under different views. The data stream was transferred from the camera to a RAID 0 volume of solid state drives (4 × Crucial M550 1TB) in real time. The raw images are finally saved in 16-bit TIFF format at giga to tens of giga voxels scale.

**Efficient GPU-accelerated SVR reconstruction.** Practically, a steepest descent method was provided in SVR, to iteratively approach a converged super-resolved solution at high efficiency:

$$\hat{\underline{I}}_m = \hat{\underline{I}}_{m-1} - \beta\left[\sum_{k=1}^{n} S_k^T O_k^T D_k^T sign(D_k O_k S_k \hat{\underline{I}}_{m-1} - \underline{P}_k)\right] \quad (2)$$

where $S_k^T, O_k^T, D_k^T$ represent the inverse operation of $S_k, O_k, D_k$, respectively. A matlab script was first developed as a proof of SVR's principle (Supplementary Notes and Supplementary Fig. S4). Using a desktop workstation with dual Intel E5-2630 v4 CPUs (no GPU involved), the processing throughput was not more than 0.3 megavoxels per second, almost 3-orders slower than the image acquisition. reconstructing tens to hundreds of gigavoxels data volume for large specimens would take an impractically long time of days. In this context, we developed a GPU-based parallel workflow to speed up the processing with near 3-orders acceleration achieved (Supplementary Table 1). Depending on the degree of

bioRxiv preprint doi: https://doi.org/10.1101/255695; this version posted January 29, 2018. The copyright holder for this preprint (which was not certified by peer review) is the author/funder. All rights reserved. No reuse allowed without permission.

parallelization and the number of views provided, the processing throughput varied from tens to hundreds of megavoxls per second, by the power of dual NVidia TESLA P100 graphical cards. For example, in single view configuration, the program explicitly finished a high-resolution reconstruction of intact heart in ~12 minutes (90 gigavoxels), a dual-color reconstruction of entire zebrafish embryo in ~4 minutes (34 gigavoxels). It should be noted that the speed can be further increased with employing more GPUs. In the multi-view SVR of thick and scattering HUVEC-HDF sprouting, 32 groups of LR images were extracted from the raw sequence of each view. The unit lateral and axial shifts were 100 nm and 558 nm, respectively. Taking the optical blurring and camera's under-sampling into account, the effective lateral and axial resolution of each LR image were around 7 μm and 26 μm, respectively, yielding ~1.1 gigavoxels SBP (voxel size 3.25*3.25*9 μm) over an ~100 $mm^3$ volume. With applying aforementioned SVR procedure, the super-resolved image $I_{single}$ under each view could be reconstructed as intermediate results. In each reconstructed $I_{\mathrm{single}}$, an increased SBP of 34 gigavoxels was presented anisotropically (0.81×0.81×4.5 μm voxel spacing). According to the reported multi-view fusion method, we interpolated all $I_{single}$ with isotropic 0.81 μm pitch size, rotated the 2nd view and registered it to the 0° reference view by iteratively matching their histograms. An initial fusion of the images was generated by taking the weighted average of the two registered views in Fourier space.

$$\hat{\underline{I}}_{(1,2),merged} = w_1 \cdot \hat{\underline{I}}_1 + w_2 \cdot \hat{\underline{I}}_{2,registered}$$

Where $\hat{\underline{I}}$ represented the Fourier transform of $\underline{I}$ and $w$ was the corresponding weights that reasonably averaged the 2 VSR views . Then this initial fusion was used for the second registration and fusion iteration, in which the reference became the fusion of first stage. By repeating this process, we obtained the fused image $I_{merged}$ that had gathered the effective information from all the SVR views[46]. This procedure could be expressed as following:

$$\hat{\underline{I}}_{(1,...j),merged} = w_{(1,..j-1)} \cdot \hat{\underline{I}}_{(1,...j-1),merged} + w_j \cdot \hat{\underline{I}}_{j,registered}$$

where $j = 3, 4$ in a 4-view SVR fusion. The weighting of the average was determined by the expected signal-to-noise ratio as following,

$$w_j = \frac{\sqrt{\left|\hat{\underline{I}}_{j,registered}\right|}}{\sqrt{\left|\hat{\underline{I}}_{(1,...j-1),merged}\right|} + \sqrt{\left|\hat{\underline{I}}_{j,registered}\right|}}, \quad w_{(1,...j-1)} = \frac{\sqrt{\left|\hat{\underline{I}}_{(1,...j-1),merged}\right|}}{\sqrt{\left|\hat{\underline{I}}_{(1,...j-1),merged}\right|} + \sqrt{\left|\hat{\underline{I}}_{j,registered}\right|}},$$

A multi-view deconvolution was applied at the last step to obtain the deblurred output, which showed a final SBP of ~190 gigavoxels with isotropically improved resolution. The implementation of SVR and mv-SVR methods were also detailed in Supplementary Notes. At present, as a proof-of-concept, the mv-SVR is based on histogram registration and weighted fusion, and had not been optimized with performance. It is noted that a more efficient bead-based registration[47] and Bayesian deconvolution[49] had been recently reported. We believe SVR

bioRxiv preprint doi: https://doi.org/10.1101/255695; this version posted January 29, 2018. The copyright holder for this preprint (which was not certified by peer review) is the author/funder. All rights reserved. No reuse allowed without permission.

also can be combined with them to obtain even better image quality and higher speed. Also, here we verify the capacity using 4-views data, and it is quite certain that the result could be increasingly optimized with more views provided[46].

**Image visualization and analysis.** The visualizations of SPIM, SLSM and confocal data were performed using Amira (Visage Imaging). Planar images were shown as their original formats, unless otherwise mentioned, with no sharpening, interpolation or registration applied. Maximum intensity projections and volume renderings were performed using the ProjectionView and Voltex functions in Amira with built-in colormaps. The long-projection neuronal tracing of clarified mouse brain was performed using Filament module in Imaris (Bitplane). See Supplementary Figures for additional details and spatiotemporal visualizations of developing zebrafish embryo, adult zebrafish fish heart and neonate mouse heart.

**Preparation of large-scale, 3D-cultured cells.** Normal Human Bronchial Epithelium (NHBE) (Lonza, Walkersville, MD) was prepared. The growth factor reduced reconstituted basement membrane (Matrigel, BD Biosciences, Bedford, MA) was used for 3-D culture experiments. Cells were seeded into 300 µl of Matrigel in liquid state and gently mixed with a pipet. Cells were then placed in a 24 well plate and incubated for 25 min at 37 °C to gelatinize. 1 ml of bronchial epithelial growth medium, BEGM (Lonza, Walkersville, MD) was added to the 24 well plate and medium was exchanged every other day. **Fluorescent staining.** Cells were stained to visualize the branching structure by direct and indirect immunofluorescent staining. For fixation, 4 % paraformaldehyde (Electron Microscopy Science, Hatfield, PA) was applied to Matrigel at room temperature for 20 minutes. After washing with PBS, PBS containing 0.5% Triton X-100 was applied for cell permeabilization for 10 minutes at 4 °C and was followed by three 10 minute washes with PBS. Then, gels were blocked with 10% goat serum and 1% goat anti mouse immunoglobulin G (Sigma-Aldrich, St. Louis, MO) in IF-buffer (0.2% Triton X-100; 0.1% BSA and 0.05% Tween-20 in PBS). As a primary antibody, rabbit E-Cadherin Monoclonal Antibody (Life technologies, Grand Island, NY) was incubated with Matrigel overnight at 4 °C and gel was rinsed three times with 10% Goat Serum for 20 minutes each. Then Alexa Fluor 555 Goat Anti-Rabbit IgG was incubated for 2 hours at room temperature followed by three 20 minutes rinsing with PBS. For nuclear staining, Dapi was incubated for 20 minutes at room temperature followed by three 20 minutes rinsing.

Human Umbilical Vein Endothelial Cells (HUVEC) were mixed with dextran-coated Cytodex 3 microcarriers at a concentration of 400 HUVEC per bead in 1 ml of EGM-2 medium. Beads with cells were shaken gently every 20 min for 4h at 37°C and 5% CO2. Beads with cells were then transferred to a 25-cm2 tissue culture flask and left for 12–16 h in 5 ml of EGM-2 at 37°C and 5% CO2. The following day, beads with cells were washed three times with 1 ml of EGM-2 and re-suspended at a concentration of 500 beads/ml in 2 mg/ml fibrinogen, 1 U /ml factor XIII and 0.04 U/ml aprotinin, 80,000 cells/ml Human Dermal Fibroblasts (HDF) at a pH of 7.4. 250 µl of this fibrinogen/bead solution was added to 0.16 units of thrombin in one well of glass-bottom 24-well plates. Fibrinogen/ HUVEC bead/ HDF cells solution was allowed to clot for 5 min at room temperature and then at 37°C and 5% CO2 for 20 min. EGM-2 was added to each well and equilibrated with the fibrin clot for 30 min at 37°C and 5% CO2. Medium was removed from the well and replaced with 1 ml of fresh EGM-2 and later was changed every other day. The co-culture assays were monitored for 7 days, then fixed and stained with Alexa Fluor 488 for imaging the cytoskeletons.

bioRxiv preprint doi: https://doi.org/10.1101/255695; this version posted January 29, 2018. The copyright holder for this preprint (which was not certified by peer review) is the author/funder. All rights reserved. No reuse allowed without permission.

**Zebrafish embryo culture.** Transgenic zebrafishes (Islet1:GFP-mlcr:DsRed and cmlc2:GFP) were raised in the zebrafish core facility of UCLA. All the experiments were performed in compliance with the approval of GLA Institutional Animal Care and UCLA IACUC protocol. To maintain transparency of zebrafish embryos, embryos were incubated with egg water containing 0.2 mM 1-phenyl-2-thio-urea (Sigma) to suppress pigmentation at 24 hpf. The live fish embryos were anaesthetized with low concentration Tricaine (0.04mg/ml, MS-222, Sigma) before they were mounted to a FEP tube for sustained imaging.

**Optical clearing of thick organs.** The adult mouse brain (Thy1-GFP-M), neonate mouse heart (wild-type, αMHCCre ; R26VT2/GK), and adult zebrafish heart (cmlc2-GFP) were originally turbid organs. As a result, tissue optical clearing need to be performed before fluorescence imaging. An organic-solvent-based clearing method (uDISCO[50]) was used to clarify the adult mouse brain and zebrafish heart, and a hydrogel-based clearing (CLARITY[2]) method was used to clarify the neonate mouse hearts.

## Acknowledgements

The authors acknowledge the contributions of R. Ardehali and K. Sereti for assistance with heart sample selection and preparation, as well as R. Kulkarni, H. Chen and K. Sung for assistance with organ clearing. The authors thank X. Wang and Y. Bu for discussions on zebrafish data analysis, and S. Dong for his assistance with instrumentation and GPU-based computation. This research has received funding support from 1000 Youth Talents Plan of China (P.F.), Fundamental Research Program of Shenzhen (P.F., JCYJ20160429182424047), the National Heart Lung and Blood Institute, R01HL111437(T.K.H.), R01HL083015 (T.K.H.), R01HL118650 (T.K.H.) and EB U54 EB0220002 (T.K.H.).

## Author Contributions

P.F. and T.K.H. conceived the idea, initiated the investigation. J.N., J.L., Y.D., Z.Y., H.Z., P.F. and T.K.H. built the system, developed the programs, acquired and processed data, and prepared the manuscript. S.L. and T.S. provided and assisted with HUVEC-HDF cell samples, M.H. provided and assisted with NHBE cell samples, and T.Y. and D.Z. provided and assisted with mouse brains. S.L., T.S., M.H., T.Y., D.Z. and C.H. all advised on image interpretation and manuscript preparation.

## Additional Information

Correspondence and requests for materials should be addressed to feipeng@hust.edu.cn (P.F.) or thsiai@mednet.ucla.edu (T.K.H.).

## References

1 Megason, S. G. & Fraser, S. E. Digitizing life at the level of the cell: high-performance laser-scanning microscopy and image analysis for in *toto* imaging of development. *Mechanisms of Development* **120**, 1407-1420, doi:10.1016/j.mod.2003.07.005 (2003).

bioRxiv preprint doi: https://doi.org/10.1101/255695; this version posted January 29, 2018. The copyright holder for this preprint (which was not certified by peer review) is the author/funder. All rights reserved. No reuse allowed without permission.


2 Chung, K. *et al.* Structural and molecular interrogation of intact biological systems. *Nature* **497**, 332 (2013).

3 Yang, B. *et al.* Single-cell phenotyping within transparent intact tissue through whole-body clearing. *Cell* **158**, 945 (2014).

4 Ragan, T. *et al.* Serial two-photon tomography for automated ex vivo mouse brain imaging. *Nature methods* **9**, 255 (2012).

5 Chalfie, M., Tu, Y., Euskirchen, G., Ward, W. W. & Prasher, D. C. Green fluorescent protein as a marker for gene expression. *Science* **263**, 802-805 (1994).

6 Pawley, J. & Masters, B. R. Handbook of biological confocal microscopy. *Optical Engineering* **35**, 2765-2766 (1996).

7 Lichtman, J. W. & Conchello, J. A. Fluorescence microscopy. *Nature methods* **2**, 910 (2005).

8 Power, R. M. & Huisken, J. A guide to light-sheet fluorescence microscopy for multiscale imaging. *Nature methods* **14**, 360 (2017).

9 Huisken, J., Swoger, J., Del Bene, F., Wittbrodt, J. & Stelzer, E. H. Optical sectioning deep inside live embryos by selective plane illumination microscopy. *Science* **305**, 1007-1009 (2004).

10 Keller, P. J., Schmidt, A. D., Wittbrodt, J. & Stelzer, E. H. Reconstruction of zebrafish early embryonic development by scanned light sheet microscopy. *science* **322**, 1065-1069 (2008).

11 Keller, P. J. *et al.* Fast, high-contrast imaging of animal development with scanned light sheet-based structured-illumination microscopy. *Nature methods* **7**, 637-642, doi:10.1038/nmeth.1476 (2010).

12 Chen, B. C. *et al.* Lattice light-sheet microscopy: imaging molecules to embryos at high spatiotemporal resolution. *Science* **346**, 1257998, doi:10.1126/science.1257998 (2014).

13 Ahrens, M. B., Orger, M. B., Robson, D. N., Li, J. M. & Keller, P. J. Whole-brain functional imaging at cellular resolution using light-sheet microscopy. *Nature methods* **10**, 413-420, doi:10.1038/nmeth.2434 (2013).

14 Susaki, E. A. *et al.* Whole-brain imaging with single-cell resolution using chemical cocktails and computational analysis. *Cell* **157**, 726-739, doi:10.1016/j.cell.2014.03.042 (2014).

15 Keller, P. J. & Ahrens, M. B. Visualizing whole-brain activity and development at the single-cell level using light-sheet microscopy. *Neuron* **85**, 462-483, doi:10.1016/j.neuron.2014.12.039 (2015).

16 Vladimirov, N. *et al.* Light-sheet functional imaging in fictively behaving zebrafish. *Nat Methods* **11**, 883-884, doi:10.1038/nmeth.3040 (2014).

17 Holekamp, T. F., Turaga, D. & Holy, T. E. Fast three-dimensional fluorescence imaging of activity in neural populations by objective-coupled planar illumination microscopy. *Neuron* **57**, 661-672, doi:10.1016/j.neuron.2008.01.011 (2008).

18 Dodt, H.-U. *et al.* Ultramicroscopy: three-dimensional visualization of neuronal networks in the whole mouse brain. *Nature methods* **4**, 331-336 (2007).

19 Lee, J. *et al.* 4-Dimensional light-sheet microscopy to elucidate shear stress modulation of cardiac trabeculation. *The Journal of clinical investigation* **126**, 1679-1690 (2016).

bioRxiv preprint doi: https://doi.org/10.1101/255695; this version posted January 29, 2018. The copyright holder for this preprint (which was not certified by peer review) is the author/funder. All rights reserved. No reuse allowed without permission.

20 Fei, P. *et al.* Cardiac Light-Sheet Fluorescent Microscopy for Multi-Scale and Rapid Imaging of Architecture and Function. *Sci Rep-Uk* **6** (2016).

21 Guan, Z. *et al.* Compact plane illumination plugin device to enable light sheet fluorescence imaging of multi-cellular organisms on an inverted wide-field microscope. *Biomedical optics express* **7**, 194-208 (2016).

22 Tomer, R., Ye, L., Hsueh, B. & Deisseroth, K. Advanced CLARITY for rapid and high-resolution imaging of intact tissues. *Nature protocols* **9**, 1682-1697, doi:10.1038/nprot.2014.123 (2014).

23 Ding, Y. *et al.* Light-sheet fluorescence imaging to localize cardiac lineage and protein distribution. *Scientific reports* **7**, 42209, doi:10.1038/srep42209 (2017).

24 Lohmann, A. W., Dorsch, R. G., Mendlovic, D., Ferreira, C. & Zalevsky, Z. Space–bandwidth product of optical signals and systems. *Journal of the Optical Society of America A* **13**, 470-473 (1996).

25 Brown, M. & Lowe, D. G. Automatic panoramic image stitching using invariant features. *International journal of computer vision* **74**, 59-73 (2007).

26 Szeliski, R. Image alignment and stitching: A tutorial. *Foundations and Trends® in Computer Graphics and Vision* **2**, 1-104 (2006).

27 Santi, P. A. *et al.* Thin-sheet laser imaging microscopy for optical sectioning of thick tissues. *BioTechniques* **46**, 287-294, doi:10.2144/000113087 (2009).

28 Buytaert, J. A. & Dirckx, J. J. Tomographic imaging of macroscopic biomedical objects in high resolution and three dimensions using orthogonal-plane fluorescence optical sectioning. *Applied optics* **48**, 941-948 (2009).

29 Glaser, A. K. *et al.* Light-sheet microscopy for slide-free non-destructive pathology of large clinical specimens. **1**, 0084 (2017).

30 Maiden, A. M., Rodenburg, J. M. & Humphry, M. J. Optical ptychography: a practical implementation with useful resolution. *Optics Letters* **35**, 2585-2587 (2010).

31 Zheng, G., Horstmeyer, R. & Yang, C. Wide-field, high-resolution Fourier ptychographic microscopy. *Nat Photonics* **7**, 739-745, doi:10.1038/nphoton.2013.187 (2013).

32 Hillman, T. R., Gutzler, T., Alexandrov, S. A. & Sampson, D. D. High-resolution, wide-field object reconstruction with synthetic aperture Fourier holographic optical microscopy. *Optics Express* **17**, 7873-7892 (2009).

33 Fangyen, C. *et al.* High-speed synthetic aperture microscopy for live cell imaging. *Optics Letters* **36**, 148 (2011).

34 Gutzler, T., Hillman, T. R., Alexandrov, S. A. & Sampson, D. D. Coherent aperture-synthesis, wide-field, high-resolution holographic microscopy of biological tissue. *Optics Letters* **35**, 1136-1138 (2010).

35 Luo, W., Greenbaum, A., Zhang, Y. & Ozcan, A. Synthetic aperture-based on-chip microscopy. *Light: Science & Applications* **4**, e261, doi:10.1038/lsa.2015.34 (2015).

36 Zheng, G., Lee, S. A., Yang, S. & Yang, C. Sub-pixel resolving optofluidic microscope for on-chip cell imaging. *Lab on a chip* **10**, 3125-3129, doi:10.1039/c0lc00213e (2010).

37 Zheng, G., Lee, S. A., Antebi, Y., Elowitz, M. B. & Yang, C. The ePetri dish, an on-chip cell imaging platform based on subpixel perspective sweeping microscopy

bioRxiv preprint doi: https://doi.org/10.1101/255695; this version posted January 29, 2018. The copyright holder for this preprint (which was not certified by peer review) is the author/funder. All rights reserved. No reuse allowed without permission.

(SPSM). *Proceedings of the National Academy of Sciences of the United States of America* **108**, 16889 (2011).

38 Luo, W., Zhang, Y., Feizi, A., Göröcs, Z. & Ozcan, A. Pixel super-resolution using wavelength scanning. *Light Science & Applications* **5**, e16060 (2016).

39 Xu, W., Jericho, M. H., Meinertzhagen, I. A. & Kreuzer, H. J. Digital in-line holography for biological applications. *Proceedings of the National Academy of Sciences of the United States of America* **98**, 11301-11305, doi:10.1073/pnas.191361398 (2001).

40 Denis, L., Lorenz, D., Thiébaut, E., Fournier, C. & Trede, D. Inline hologram reconstruction with sparsity constraints. *Optics Letters* **34**, 3475-3477 (2009).

41 Greenbaum, A. *et al.* Increased space-bandwidth product in pixel super-resolved lensfree on-chip microscopy. *Scientific reports* **3**, doi:10.1038/srep01717 (2013).

42 Elad, M. & Hel-Or, Y. A fast super-resolution reconstruction algorithm for pure translational motion and common space-invariant blur. *IEEE Transactions on Image Processing A Publication of the IEEE Signal Processing Society* **10**, 1187 (2001).

43 Farsiu, S., Robinson, M. D., Elad, M. & Milanfar, P. Fast and robust multiframe super resolution. *Image Processing IEEE Transactions on* **13**, 1327-1344 (2004).

44 Vandewalle, P., Süsstrunk, S. & Vetterli, M. A Frequency Domain Approach to Registration of Aliased Images with Application to Super-resolution. *EURASIP Journal on Advances in Signal Processing* **2006**, 1-15, doi:10.1155/asp/2006/71459 (2006).

45 Greenbaum, A., Sikora, U. & Ozcan, A. Field-portable wide-field microscopy of dense samples using multi-height pixel super-resolution based lensfree imaging. *Lab on a chip* **12**, 1242-1245, doi:10.1039/c2lc21072j (2012).

46 Swoger, J., Verveer, P., Greger, K., Huisken, J. & Stelzer, E. H. Multi-view image fusion improves resolution in three-dimensional microscopy. *Optics Express* **15**, 8029-8042 (2007).

47 Saalfeld, S. Software for bead-based registration of selective plane illumination microscopy data. *Nature methods* **7**, 418 (2010).

48 Paxinos, G. & Franklin, K. B. *The mouse brain in stereotaxic coordinates*. (Gulf Professional Publishing, 2004).

49 Preibisch, S. *et al.* Efficient Bayesian-based multiview deconvolution. *Nature methods* **11**, 645-648, doi:10.1038/nmeth.2929 (2014).

50 Pan, C. *et al.* Shrinkage-mediated imaging of entire organs and organisms using uDISCO. *Nature methods* **13**, 859-867, doi:10.1038/nmeth.3964 (2016).

bioRxiv preprint doi: https://doi.org/10.1101/255695; this version posted January 29, 2018. The copyright holder for this preprint (which was not certified by peer review) is the author/funder. All rights reserved. No reuse allowed without permission.

# Figures and Captions

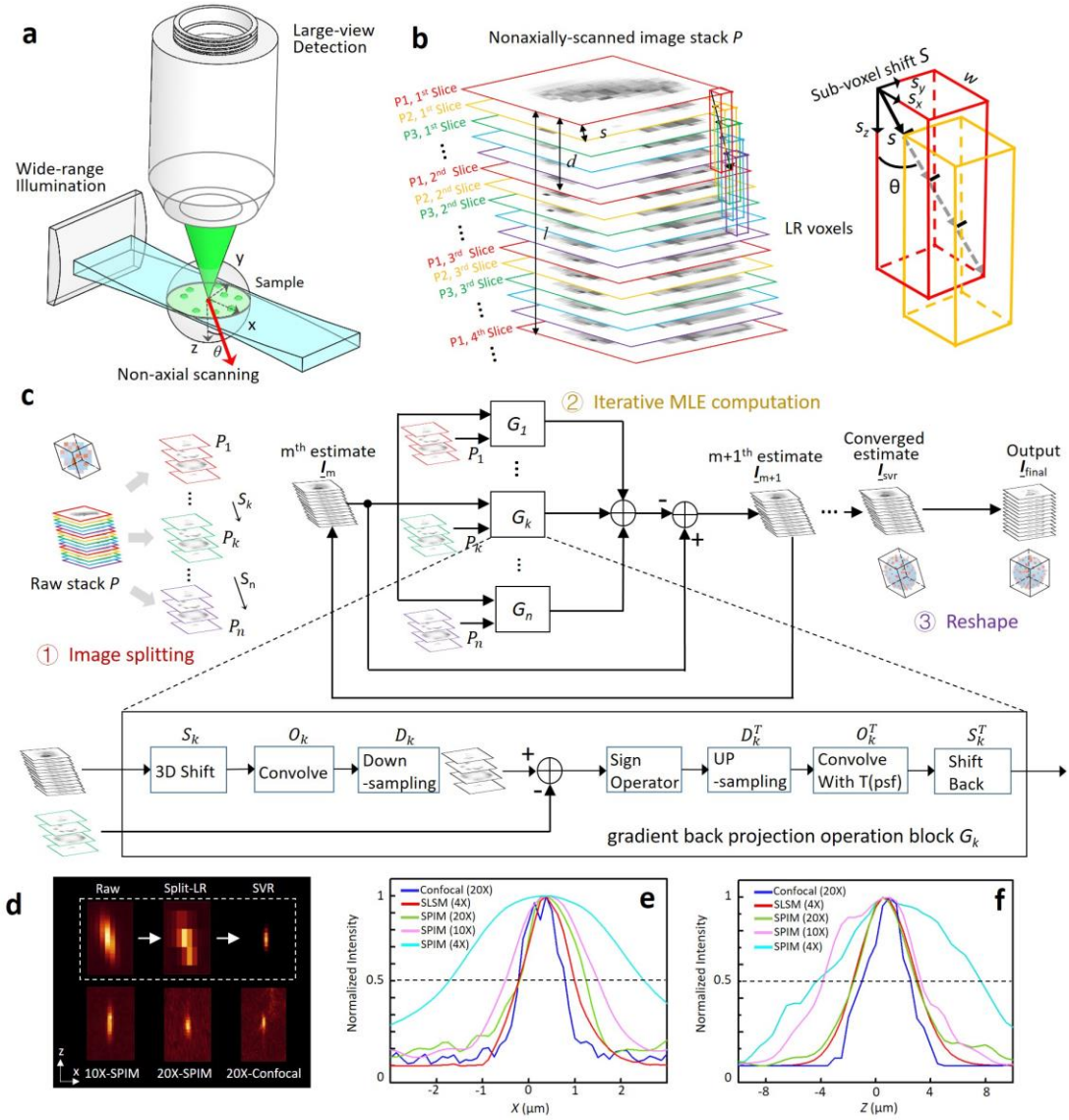


**Figure 1. Principle of SLSM**. **a**, SLSM geometry with wide laser-sheet illumination and large-FOV detection. The sample is scanned along a direction (red arrow) with deviation angle $\theta$ being 10 to 20 degree to the z axis. **b,** A sequence of low-resolution, spatially-modulated images recorded under a high frame rate. The step-size $s$ is much smaller than the laser-sheet longitudinal extent $l$ ($1/e^2$). The raw image stack is split into multiple sub-stacks (illustrated by different colors), with voxel depth $d$ being a third of laser-sheet thickness $l$. Each low-resolution sub-stack $P_k$ is correlated to the 1st reference stack $P_1$ (red color), with non-axial, sub-voxel shift $s_k = (k-1) * s$. For instance, $P_2$ (yellow color) can be registered to $P_1$ with unit displacement $s$, which consists of three-directional components $s_x$, $s_y$ and $s_z$ simultaneously. **c,** Block diagram of iterative SVR procedure. The spatially-correlated, wide-view, low-resolution stacks (step 1) are inputted into a maximum-likelihood-estimation (step 2) to iteratively reconstruct a voxel-

bioRxiv preprint doi: https://doi.org/10.1101/255695; this version posted January 29, 2018. The copyright holder for this preprint (which was not certified by peer review) is the author/funder. All rights reserved. No reuse allowed without permission.

super-resolved image. Block $G_k$ represents a gradient back-projection operator that compares the $k_{th}$ LR image to the estimate of the HR image in the $m_{th}$ steepest descent iteration. At final step 3, a voxel re-alignment is applied to recover the accurate shape of the sample from the slight deformation caused by the tilted scan. **d,** Imaging 500 nm fluorescent beads using：SLSM (4×/0.13 DO/0.022 NA sheet-illumination), SPIM (10×/0.3 DO/0.04 NA sheet-illumination, 20×/0.45 DO/0.06 NA sheet-illumination), and confocal microscope (Zeiss LSM 510, 20×/0.7 objective). The x-z planes of the bead are shown to compare the lateral and axial resolving power of different methods. **e** and **f**, Intensity plots of linecuts (as shown in a–d) through the lateral and axial extents of the bead for each method, with 50% intensity level (dashed line) shown for estimation of the FWHM.

bioRxiv preprint doi: https://doi.org/10.1101/255695; this version posted January 29, 2018. The copyright holder for this preprint (which was not certified by peer review) is the author/funder. All rights reserved. No reuse allowed without permission.

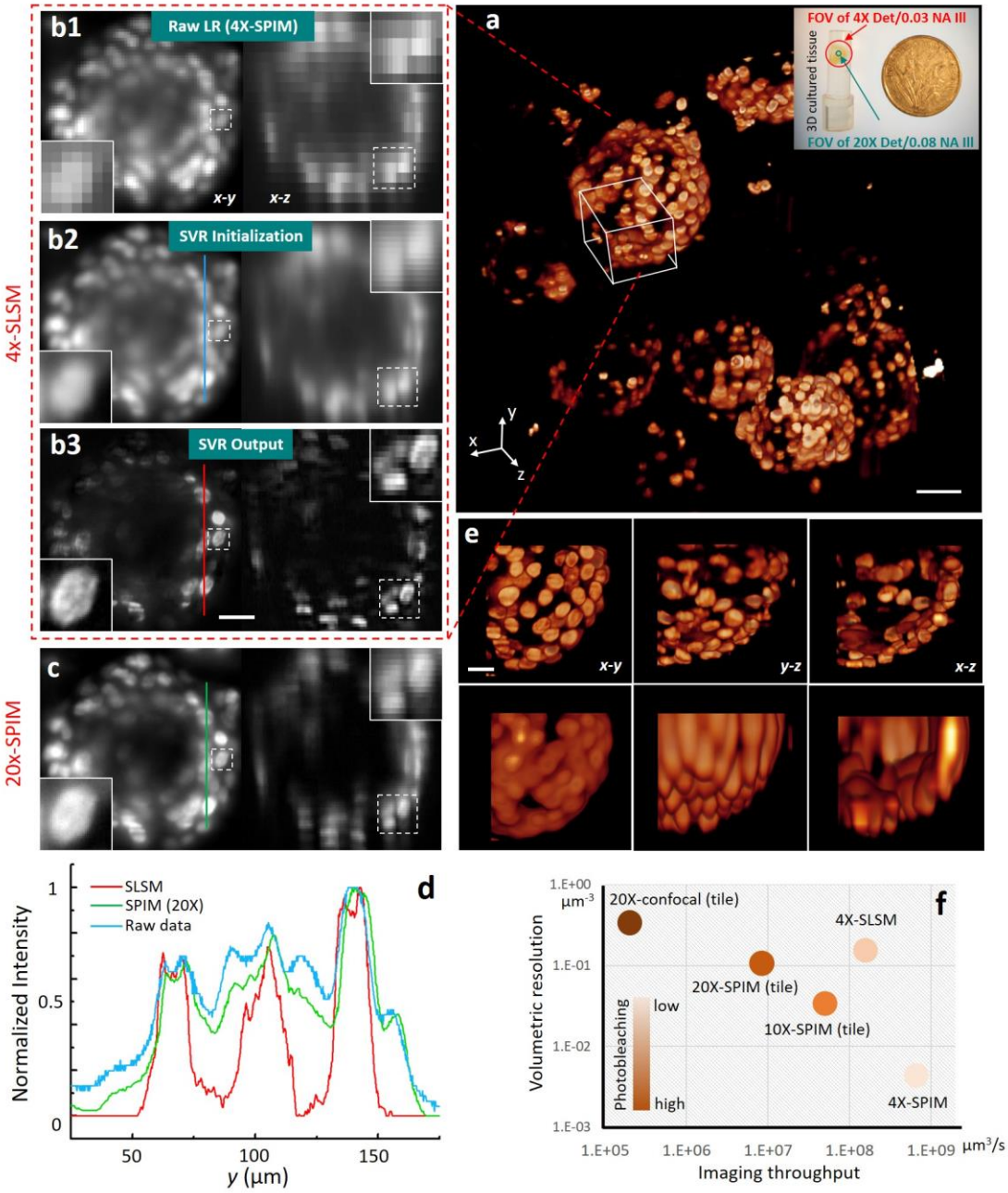


**Figure 2. SLSM demonstration of 3D-cultured NHBE cells. a,** NHBE cell spheroids three-dimensionally cultured in a piece of Matrigel substrate. The cells are fluorescently labelled by DAPI nuclear staining for SLSM reconstruction. **b1,** Low-resolution raw image of a selected cell spheroid (1st out of 64 groups), captured under illumination /detection NA of 0.022 and 0.13, with a voxel size of 1.625*1.625*6 μm. Vignette views show a single cell nucleus. **b2,** The initial estimate of SVR computation, which is a ×4 interpolation of b1. **b3,** Our final SVR reconstruction of the same region, with a reconstructed voxel size of 0.41*0.41*1.5 μm. The features of cell nucleus are recovered from blurring and pixelation, with the chromatin becoming discernable. **c**, Images of the same cell spheroid taken by SPIM using 20X/0.45 objective and 0.06 NA illumination, for comparison. **d,** Intensity plot of linecuts (shown in **b**

bioRxiv preprint doi: https://doi.org/10.1101/255695; this version posted January 29, 2018. The copyright holder for this preprint (which was not certified by peer review) is the author/funder. All rights reserved. No reuse allowed without permission.

and **c)** for each setting, indicating that SVR provides substantively improved contrast and resolution. **e,** Volume renderings in the raw mode and SVR reconstruction, comparing the 3-D localization accuracy of single cells in a self-assembled spheroid. Scale bars: 20 μm except 5 μm in insets. **f,** Comparison of imaging resolution, speed and photobleaching by 4×-SPIM, 10×-SPIM tile imaging, 20×-SPIM tile imaging, 20×confocal and 4×SLSM. The achieved effective throughputs are 2.7 mega, 1.7 mega, 0.9 mega, 0.07 mega and 24 mega SBP per second, respectively.

bioRxiv preprint doi: https://doi.org/10.1101/255695; this version posted January 29, 2018. The copyright holder for this preprint (which was not certified by peer review) is the author/funder. All rights reserved. No reuse allowed without permission.

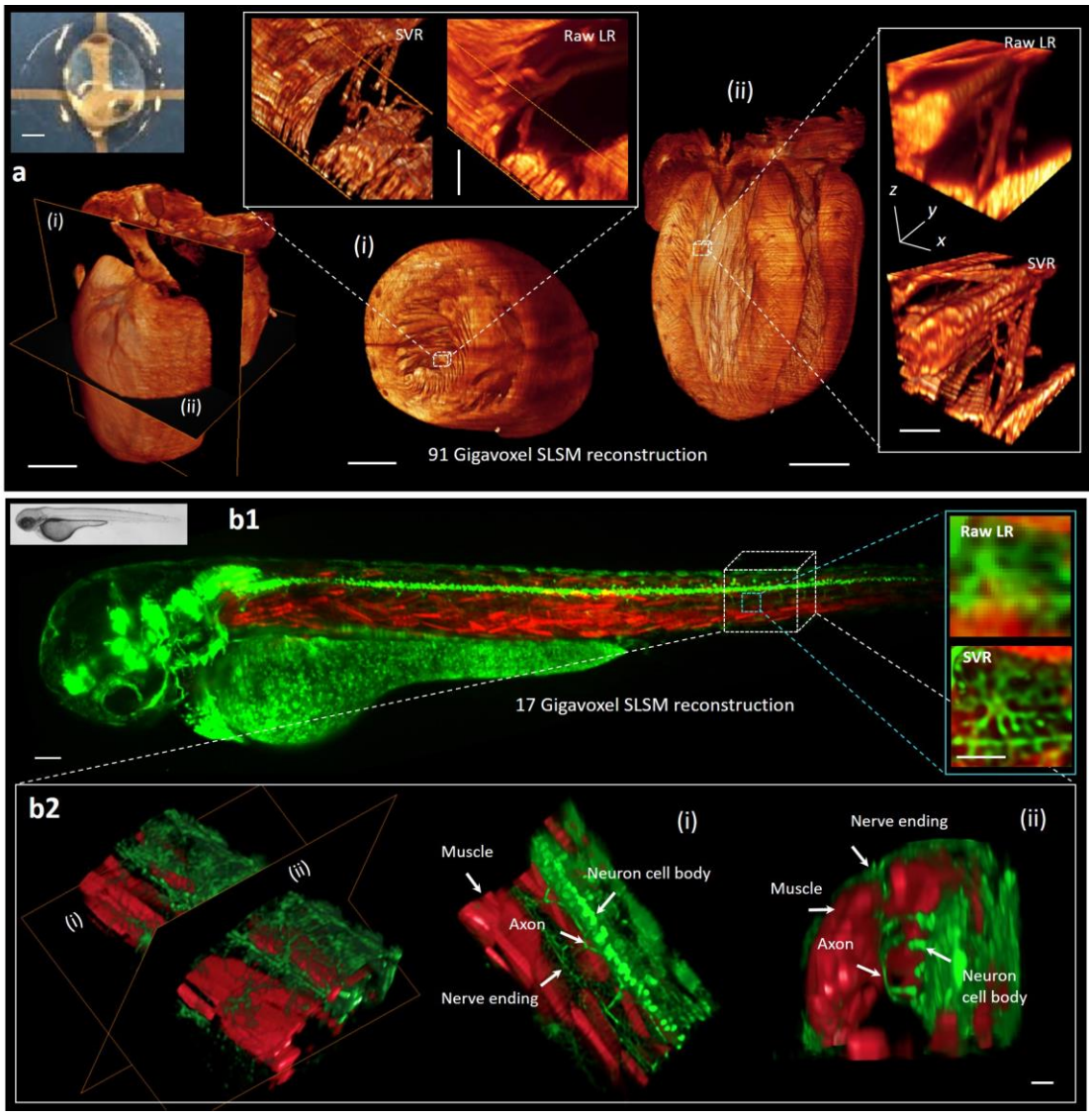


**Figure 3. Rapid high-throughput volumetric imaging of whole organisms via SLSM. a,** 90 gigavoxel SVR reconstruction of an optically-cleared intact mouse heart (neonate day 1, inset picture) with endogenous autofluorescence. Magnified views of the slices along the indicated coronal and axial planes (i and ii) reveal that SVR procedure substantively improves the visualization of cardiomyocytes, as compared to the raw images. The image acquisition and SVR reconstruction time of the entire heart is around 4 minutes and 12 minutes, respectively. Scale bars are 1 mm, except 50 μm in the magnified views. **b,** Two-color, 34 gigavoxel SVR reconstruction of an anaesthetized live zebrafish embryo (3 d.p.f.) tagged with gfp-islet at motor neurons and dsred-mlcr at somite fast muscle. **b2,** Magnified volume rendering in SVR reconstruction of a section of fish somite, unravelling how the motor neurons interplay with the muscles during developement. Images on the right show slices through the somite along the planes shown in the image on the left. The SLSM image acquisition is finished in 120 seconds for dual colors, followed by a 200-seconds GPU-based processing. Scale bars are 100 μm in the whole embryo image and 20 μm in the magnified views.

bioRxiv preprint doi: https://doi.org/10.1101/255695; this version posted January 29, 2018. The copyright holder for this preprint (which was not certified by peer review) is the author/funder. All rights reserved. No reuse allowed without permission.

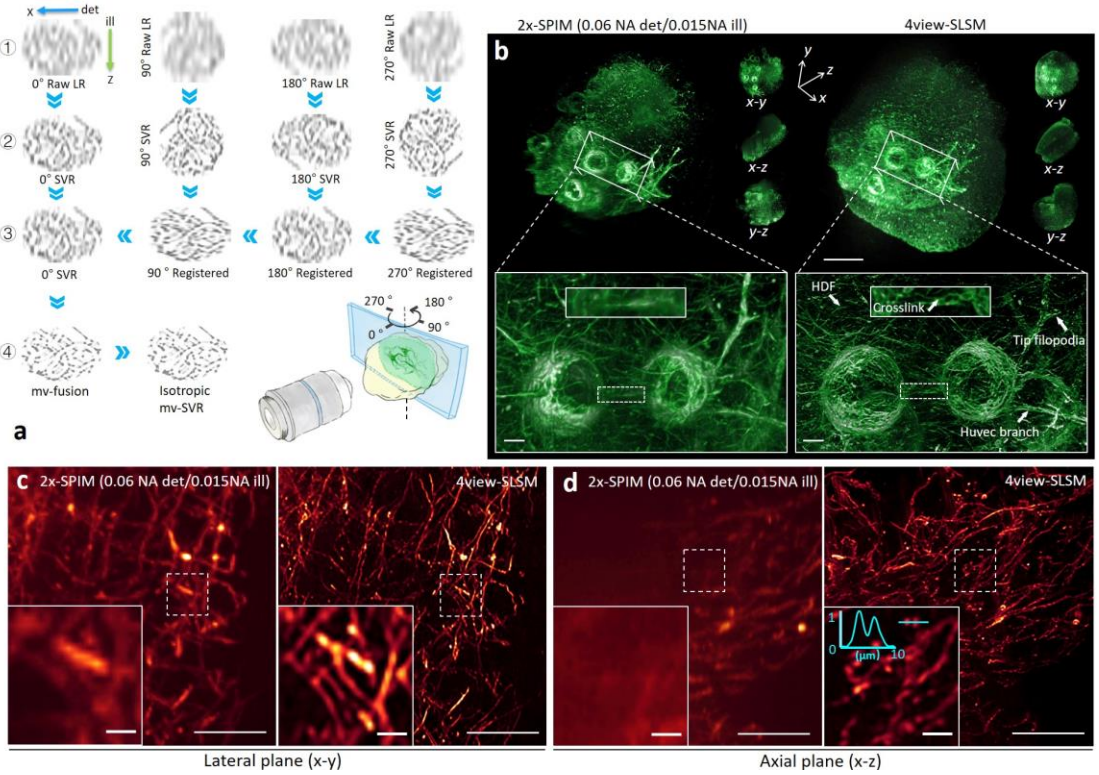


**Figure 4. mv-SLSM for three-dimensional isotropic imaging of large, scattering HUVEC-HDF cell sprouting network. a,** The strategy of mv-SVR procedure contains 1. image acquisition under multiple views; 2. SVR computation for each view; 3. image registration in 3D space, and 4. weighted mv-SVR fusion plus a final deconvolution. **b,** 3-D reconstruction of the cells by single-view SPIM (2×/0.06 DO/0.015 NA sheet-illumination ) and 4view-SLSM using the same optics. The system's SBP of SPIM is 1.1 gigavoxels for the entire sample, whereas 4view-SLSM creates 190 gigavoxels SBP that renders a higher-resolution and more complete sample structure across an ~100 $mm^3$ large FOV. Vignette high-resolution views compares the visualization of HUVEC branch, tip filopodia, and HDF co-localization (white arrowheads). **c, d,** MIPs of supporting HDF cells in x-y and x-z planes. mv-SVR reconstruction enables clear identification of single fiber sprouting (right columns in **c, d**) which however remains very fuzzy in single-view SPIM image (left columns in **c, d**). The intensity plot of the blue linecut (insets in **d**) indicates a small resolvable distance of ~1.6 μm. Besides isotropic resolution enhancement, mv-SVR reconstruction also restores the highly scattered area that is originally subject to severe signal loss in single-view image (left area in **d**). Scale bars are 1 mm in **a-b**， except 100 μm in the magnified views, 100 μm in **c–d**, except 10 μm in magnified vignette views.

bioRxiv preprint doi: https://doi.org/10.1101/255695; this version posted January 29, 2018. The copyright holder for this preprint (which was not certified by peer review) is the author/funder. All rights reserved. No reuse allowed without permission.

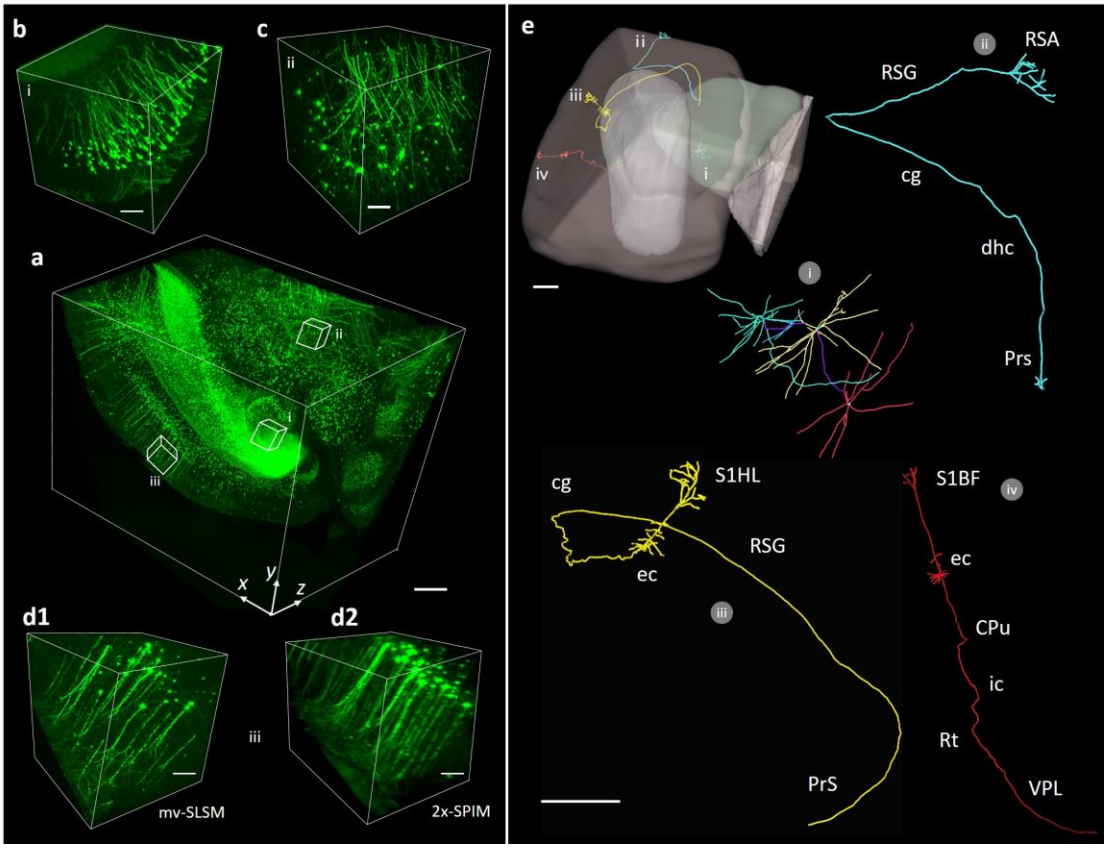


**Figure 5. Three-dimensional neuronal mapping of adult mouse brain via 8 view-SLSM. a,** Isotropic sub-voxel-resolved volume rendering of an optically-cleared Thy1-GFP-M mouse brain block (350 gigavoxels scale). Scale bar, 500 μm. **b, c, d1**, High-resolution volumetric views of the hippocampus, thalamus and cortex regions, respectively. **d2**, The cortex reconstructed by regular SPIM with 4×/0.13 DO plus 0.022 NA plane-illumination, for comparison. Scale bar, 100 μm. **e**, Analysis of neural structures and connectivity. Three clustered astrocyte neurons in the thalamus region are segmented with different colors encoded in (i). Three registered projection neurons across the brain block are annotated according to mice brain atlas (ii, iii, and iv). Abbreviations: cg, cingulum; ec, external capsule; dhc, dorsal hippocampal commissure; CPu, caudate putamen; ic, internal capsule; Rt, reticular thalamic nucleus; Prs, presubiculum; RSG, retrosplenial granular cortex; S1HL, primary somatosensory cortex hindlimb; RSA, retrosplenial agranular cortex. Scale bar, 500 μm.